FINAL REPORT

Award No.: 0348286 Amount: $400,000 Period of support: 01/30/2004–01/31/2010

Title: **CAREER: Advanced Temperature Compensation Techniques for Integrated Bulk-Mode Micro and Nano Mechanical Resonators**

The main goals of this research project were the design, fabrication and modeling of temperature-compensated, high-*Q* bulk-mode micro- and nano-electromechanical resonators with integrated transducers with resonant frequencies into the UHF frequency range. The main results achieved to date are summarized below.

1. Analytical and numerical models of SiBARs

Much research activity in recent years has been directed at the development of bulk acoustic resonators that are compatible with standard integrated circuit technologies. In this respect, capacitive resonators [1–3] offer a particularly attractive option, since they can be made entirely of materials that are used routinely in IC fabrication processes, resulting in significant advantages in terms of ease of integration and cost savings.

Disk resonators were among the first examples of devices of this type [1], but more recently width-extensional-mode resonators based on an alternative, rectangular-bar geometry were demonstrated [2][3]. In this report, resonators of this type will be referred to as silicon bulk acoustic resonators, or SiBARs. The basic structure of a SiBAR is schematically shown in Fig. 1: the resonating bar element is placed between two electrodes, supported by two thin tethers. A DC polarization voltage applied between the resonator and the electrodes generates an electrostatic field in the capacitive gaps. When an AC voltage is applied to the drive electrode, the electrostatic force applied to the corresponding face of the resonator induces an acoustic wave that propagates through the bar. Small changes in the size of the capacitive gap on the other side of the device induce a voltage on the sense electrode, whose amplitude peaks near the mechanical resonant frequencies of the bar.

SiBARs offer several potential advantages over their disk-shaped counterparts, the most important of which is that the electrostatic transduction area can be increased without changing the main frequency-setting dimension, resulting in significantly lower motional resistance while maintaining high *Q* values [3].

While the behavior of SiBARs is well understood in broad, qualitative terms, a major obstacle to the design of high performance devices is a lack of sufficiently accurate analytical or numerical models. For example, prior to this research work there was no quantitative analysis of how exactly the dimensions of a SiBAR affect its insertion loss. Even the computation of the resonant frequencies was based on approximate formulae that can be quite inaccurate, especially in the case of an anisotropic material such as single-crystal silicon.

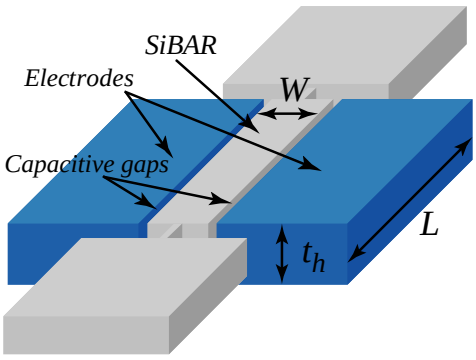

Figure 1: Structure of a SiBAR.

Under this research project we developed two new SiBAR models, one analytical and the other numerical, that are significantly more accurate than previously available models. The analytical model is obtained from an approximate solution to the linear elastodynamics equations that satisfies the boundary conditions imposed by the SiBAR geometry. The mathematical details of this derivation are omitted from this report, but

can be found in [4]. In the end, the analytical model yields a relation between v, the propagation velocity of elastic waves inside the SiBAR, and the ratio $\xi = t_h/\lambda_z$, where t_h is the thickness of the SiBAR (see Fig. 1) and λ_z is the elastic wavelength. This relation defines a function $v = v(\xi)$ that has multiple branches. To each point (ξ, v) that lies on a branch of this function there corresponds an acoustic wave that propagates across the resonator.

Figure 2 shows the graph of $v(\xi)$ for single-crystal silicon, when the x and z reference axes are aligned with the and $\langle 0\bar{1}1 \rangle$ and $\langle 011 \rangle$ crystallographic directions, and the y axis with the $\langle 100 \rangle$ direction. Only the first four of infinitely many branches of $v(\xi)$, or dispersion curves, are shown in the figure. It should be pointed out that those curves depend only on the properties of the material, and not on the geometry of the resonator.

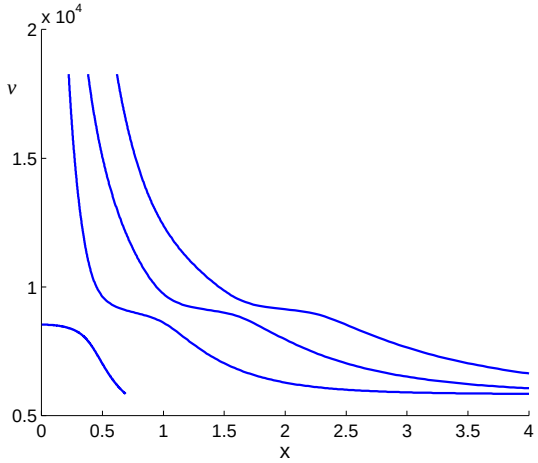

Figure 2: Propagation velocity of acoustic waves along the $\langle 011 \rangle$ crystallographic direction in a (100) silicon wafer (c_{22} = 165.7, c_{33} = 194.4, c_{23} = 63.9, c_{44} = 79.6 GPa).

Once $v(\xi)$ has been obtained, it is straightforward to relate it to the resonant frequencies of a resonator of given dimensions through the following relationship

$$f = \frac{1}{\lambda_z} v(\xi) = \frac{n_z}{2W} v(n_z t_h / 2W)$$

where n_z is the order of the resonant mode and W is the resonator width (see Fig. 1). Therefore the relationship between the resonator dimensions and its resonant frequencies can be obtained from $v(\xi)$ simply by changing the scales on the v and ξ axes.

To complement to the analytical model described above, we also developed a SiBAR model for the ANSYS simulator that accounts for both the finite length of the resonator and the electromechanical transduction in the capacitive gaps, which is an integral part of the device behavior.

The orthotropic SOLID95 model is used for the resonating bar. Electromechanical transduction is modeled with two arrays of TRANS126 elements generated by the EMTGEN macro after the bar has been meshed. A number of resistors and capacitors model the test setup used for resonator testing and characterization [3]. The equivalent schematic diagram of the complete ANSYS model is shown in Fig. 3: C_s and C_d model the gap capacitances, C_{ps} and C_{pd} the parasitic pad capacitances, and R_S and R_L the internal resistances of the test instruments.

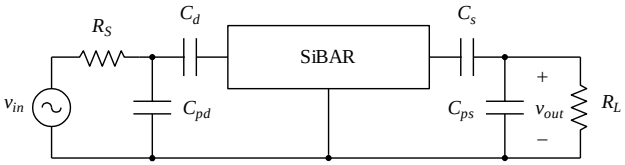

Figure 3: Equivalent circuit of the ANSYS model, including test setup.

Each simulation of the ANSYS model consists of a static analysis, which accounts for the effect of the DC polarization voltage, followed by a harmonic analysis. The simulation results include the values of all the node voltages, which makes it possible to generate plots of the voltage gain $A_v = v_{out} / v_{in}$ over the given range of frequencies. Many parameters related to the resonator performance can then be evaluated based on the location and magnitude of the peaks in the graph of $|A_v|$, including the effects of the resonator dimensions, the polarization voltage and the magnitude of the capacitive gaps not only on the resonant frequency, but also on the insertion loss.

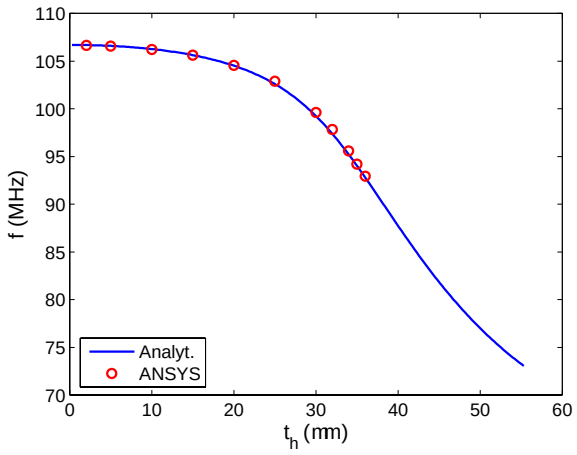

Figure 4: Resonant frequency vs. SiBAR thickness.

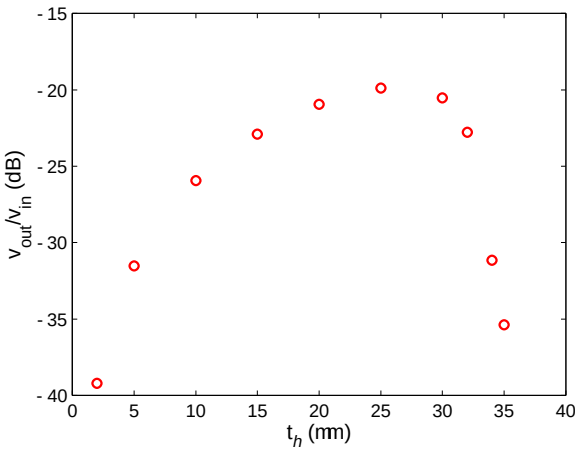

Figure 5: Plot of voltage gain vs. SiBAR thickness obtained from ANSYS simulations.

To illustrate the model's capabilities, we present the results of the simulations of a set of SiBARs having the same length (400 μm) and width (40 μm), but varying thickness. The thickness values were chosen so that the main resonant peak would fall on the first dispersion curve of Fig. 2. Figure 4 compares the values of the resonant frequency obtained from the ANSYS simulations with those predicted by the analytical model: it can be seen that the two models are in excellent agreement.

The plot of the simulated values of $|A_v|$ for the same set of SiBARs is shown in Fig. 5. As can be seen in the figure, at first the magnitude of the voltage gain increases with the thickness of the device, because of the corresponding increase in the capacitive transduction area. Beyond a certain point, however, further increases in the thickness actually cause the voltage gain to decrease. This phenomenon can be explained, at least in part, by a decrease in the efficiency of the electrostatic transduction in the capacitive gaps due to deterioration of the mode shape [5].

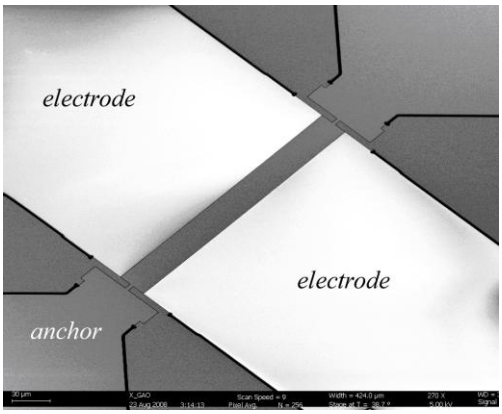

Figure 6: SEM view of a SiBAR fabricated in 10 μm thick SOI with a capacitive gap of 300 nm.

Both models were validated against measurements taken on SiBARs of various dimensions fabricated in 10 μm thick SOI. Device definition includes sub-micron trench formation using DRIE, followed by 3 μm wide peripheral trench etching, and HF release. A SEM micrograph of a sample device fabricated with this process is shown in Fig. 6. Table I compares the values of the resonant frequencies predicted by both models with those obtained from device measurements. The table shows also the relative error incurred when the approximate formula

$$f = \frac{n_z}{2W}\sqrt{\frac{E}{\rho}} \qquad (1)$$

is used to estimate the resonant frequency of the SiBAR [3]. In all models, the value of W was set equal to the measured width of the device, so that the comparison would not be affected by process variations. In (1), the value of E was set to 169 GPa. It is readily seen that the values of the resonant frequencies predicted by the models described in this paper are substantially more accurate than those given by (1), and that the error associated with the latter formula grows as the ratio $\xi = t_h/\lambda_z = n_z t_h/2W$ increases. This is consistent with the relationship between resonant frequency and SiBAR thickness predicted by both

Table I: Computed and measured resonant frequencies of SiBARs

Length (μm)	*Width (drawn) (μm)*	*Width (meas.) (μm)*	*Mode order (n_z)*	*Res. freq. (meas.) (MHz)*	*Analytical model*		*ANSYS model*		*Equation (1)*	
					Freq. (MHz)	*Error (%)*	*Freq. (MHz)*	*Error (%)*	*Freq. (MHz)*	*Error (%)*
310	40	39.97	1	106.308	106.34	0.03	106.23	-0.07	106.5	0.18
			3	299.082	297.92	-0.40	297.85	-0.41	319.61	6.86
400	40	39.86	1	106.5	106.6	0.09	106.59	0.08	106.8	0.28
216	27	26.94	1	157.064	156.84	-0.14	156.86	-0.13	158.1	0.66
270	27	26.96	1	157.062	156.73	-0.21	156.74	-0.20	157.9	0.53
240	24	23.91	1	176.452	176.12	-0.19	176.17	-0.16	178.1	0.93
200	20	19.90	1	210.628	209.97	-0.31	210.06	-0.27	214	1.6

models (see Figs. 2 and 4), which show a gradual decrease in the resonant frequency of the device as its thickness increases.

2. Effect of phonon interactions on limiting the *fQ* product of micromechanical resonators

Several dissipative mechanisms limit the *Q* of an electromechanical resonator [3][6] [7][8]. Among those, some can be minimized and even eliminated through proper design (e.g. clamping loss [8]). However, some energy dissipation mechanisms are intrinsic to the resonating material. The "intrinsic *Q*" of a resonator is defined as

$$Q = 2\pi \frac{\text{Energy stored}}{\text{Energy dissipated per cycle of oscillation}} \tag{2}$$

For an acoustic wave propagating in solids, the sound abortion coefficient $\alpha(\omega)$, defined as [9]

$$\alpha(\omega) = \frac{1}{2}\frac{\text{Mean energy dissipated}}{\text{Energy flux in the wave}} \tag{3}$$

is a measurable quantity and describes the variation in the wave amplitude with propagation distance. Therefore, by definition *Q* and $\alpha(\omega)$ are related through

$$Q = 2\pi \frac{\omega}{2\alpha(\omega)V_a} \tag{4}$$

where V_a is the wave velocity and ω is the angular resonance frequency. A figure of merit for micromechanical resonators is the *fQ* product. Using (4), we have

$$fQ = \frac{\omega^2}{2\alpha(\omega)V_a} \tag{5}$$

The fundamental intrinsic dissipation mechanisms limiting the *fQ* product of resonators consist of thermoelastic, phonon-electron, and phonon-phonon interactions (see Table II). Among these, the phonon-phonon dissipation is the dominant intrinsic loss mechanism in semiconducting and insulating resonators at room temperature. In our research we focused on the phonon-phonon dissipations and showed that at room temperature, the *fQ* product of a micromechanical resonator due to this intrinsic dissipation mechanism is frequency dependent.

Dissipation due to phonon-phonon interactions

Two different approaches have been taken to describe the physics of ultrasonic attenuation due to the interaction of an acoustic wave with thermal phonons:

Table II: Simplified expressions for α(ω) and f.Q (ω: acoustic angular frequency, ρ: density, V_a: acoustic velocity, κ: thermal conductivity, β: thermal expansion coefficient, σ: electrical conductivity, m_e: electron mass, ε_F: Fermi energy, e: electron charge, C_v: volumetric heat capacity, T: absolute temperature, γ: Grüneisen parameter, h: Planck constant, and K: Boltzmann constant).

	Thermoelastic Dissipation	**Phonon-electron Dissipation**	**Phonon-phonon Dissipation**
α	$\alpha = \frac{\kappa T \beta^2 \rho \omega^2}{18 V_a^3} \quad \omega\tau^* < 1$	$\alpha = \frac{4\varepsilon_F m_e \sigma}{15 \rho e^2 V_a^3}\omega^2$	$\begin{cases} \alpha(\omega) = \frac{C_v T \gamma^2 \tau}{2\rho V_a^3 (1+(\omega\tau)^2)}\omega^2 & \omega\tau < \\ \alpha(\omega) = \frac{\pi^5 \gamma^2 K^4 T^4}{30 \rho V_a{}^6 h^3}\omega & \omega\tau > 1 \end{cases}$
f. Q	$f.Q_{TED} = \frac{9V_a^2}{\kappa T \beta^2 \rho}$	$f.Q_{phe} = \frac{15\rho e^2 V_a^2}{8\varepsilon_F m_e \sigma}$	$\begin{cases} f.Q_{PhP} = \frac{\rho V_a^2 (1+(\omega\tau)^2)}{C_v T \gamma^2 \tau} & \omega\tau < 1 \\ f.Q_{PhP} = \frac{15\rho V_a{}^5 h^3}{\pi^5 \gamma^2 K^4 T^4}\omega & \omega\tau > 1 \end{cases}$
marks	Negligible in semiconductor with proper design. Dominant intrinsic source of loss in metals.	Negligible in insulators and doping dependent in semiconductors at room temperature.	Dominant intrinsic loss in semiconductors and insulators

a) In the approach that was first introduced by Akheiser [10], the sound wave is regarded as a macroscopic strain field in the crystal. Since the frequency of thermal phonons depends on the strain, the thermal equilibrium is disturbed [7], leading to ballistic transport of phonons between hot and cold regions (as opposed to the diffusive transport of heat in the thermoelastic dissipation). The process of restoring the thermal equilibrium to the phonon gas is accompanied by dissipation of energy from the acoustic wave. The response of the phonon system to the acoustic wave is calculated by means of the phonon Boltzmann equation [11].
b) An alternative approach was given by Landau and Rumer [12]. Here, the acoustic wave is regarded as a parallel beam of low-energy phonons. Because of an-harmonic terms in the Hamiltonian of the crystal, interactions between different modes are possible and the rate at which the acoustic phonons are scattered is calculated by the perturbation theory [13].

Both approaches are valid, subject to some assumptions on the wavelength of the propagating acoustic wave and on the life time of thermal phonons (which depends on the temperature of the material). In our research we focused on the nature of the acoustic attenuation *at room temperature* (300 ºK) and considered only the frequency dependency of phonon-phonon dissipation.

Akheiser Regime: If the acoustic wavelength (λ) is considerably larger than the mean free path of phonons ($\omega << 1/\tau$), we can assume that the acoustic wave is interacting with the whole ensemble of thermal phonons. Therefore, *locally* changing the phonon frequencies and perturbing the phonon distribution function away from its equilibrium Planck form. This range ($\omega << 1/\tau$) is known as the Akheiser regime. In the Akheiser regime, the wave equation can be formulated based on the modified Hooke's law, proposed by Zener [14], and the second law of Newton as follows:

$$c_R \cdot \frac{\partial^2 V}{\partial z^2} + \eta \cdot \frac{\partial^3 V}{\partial t \cdot \partial z^2} - \frac{\eta}{c_U} \cdot \rho \cdot \frac{\partial^3 V}{\partial t^3} = \rho \cdot \frac{\partial^2 V}{\partial t^2} \tag{6}$$

where c_R and c_U are the relaxed and un-relaxed elastic stiffness constants, η is the *effective* viscosity of the acoustic material, and V is the velocity. Assuming a plane wave solution $V = e^{j(\omega t - kz)}$ and considering the acoustic absorption, we have: $k = \chi - j\alpha(\omega)$. In all practical cases $\alpha(\omega)$ is very small compared to χ and ω [10]. Therefore:

$$\frac{\omega}{\chi} = \sqrt{\frac{c_R}{\rho}} = V_a, \tag{7}$$

$$\alpha(\omega) = \frac{\omega^2 \cdot \eta \cdot (c_U - c_R)}{2 \cdot V_a \cdot c_U \cdot c_R} \tag{8}$$

For *longitudinal* acoustic waves in Akheiser regime, the acoustic attenuation is proportional to ω^2, hence the fQ_{PhP} product is constant (see eq. (5)). For *transverse* waves in the Akheiser range, $\alpha(\omega)$ is theoretically proportional to $\omega^{1.75}$ [16]. Therefore, fQ_{PhP} has a slight frequency dependency ($fQ_{PhP} \propto \omega^{0.25}$). A dependence of this kind has been observed in many crystals [11], and may be due to the presence of impurities, which influences heavily the attenuation in transverse acoustic waves but may affect longitudinal waves only slightly [17].

Landau-Rumer Regime: When λ is less than the phonon mean free path, the acoustic quanta interact with individual lattice phonons. In the Landau-Rumer regime ($\omega >> 1/\tau$), acoustic attenuation is mainly due to three-phonon interactions and can be shown to be linearly proportional to ω [12]. Therefore, the fQ product will not be constant but *will increase linearly* with ω (Table II).

Landau-Rumer Effect at Room Temperature: The transition from Akheiser to Landau-Rumer regime occurs at $\omega_\tau = 1/\tau$, which can be estimated as

$$\omega_\tau = \frac{C_v V_D^2}{3n\kappa} \qquad \left(\frac{3}{V_D^3} = \frac{1}{V_l^3} + \frac{2}{V_t^3} \right) \tag{9}$$

where V_D, V_l, and V_t are the mean Debye, longitudinal and transverse velocities, respectively. We define n as a correction factor, which is close to 1 for transverse waves. The reason for this is that for transverse sound waves τ is usually assumed to be close to the thermal relaxation time τ_C. For longitudinal waves, the direct interaction with thermal phonons is forbidden and therefore, τ becomes greater (n is close to 2).

The condition $\omega >> 1/\tau$ is met more easily at low temperatures, as τ increases rapidly with falling temperature [17]. At room temperature, for most semiconductors, ω_τ falls in the GHz range (1-20 GHz) [18]. Interestingly, for an acoustic wave propagating in <100> direction in silicon, τ is an order of magnitude larger than that of the other directions. This has been experimentally verified in [17], where the value of τ was extracted from the kink in the measured frequency-dependent acoustic attenuation curve. The significance of this effect is pronounced at frequencies above $\omega_\tau = 2\pi f_\tau = 1/\tau$, where fQ_{PhP} increases with frequency (Fig. 7). For silicon in <100> direction, f_τ is ~700 MHz.

To understand the reason for the relatively large phonon relaxation time of longitudinal waves propagating in <100> direction in silicon, one has to rely on the an-harmonic phonon decay model of Landau and Rumer, which accounts only for the types of phonon collisions that are allowed by the crystalline anisotropy [9],[19]. In <100> direction in silicon, out of all allowed interactions, only those with transverse phonons contribute to absorption (or acoustic attenuation). The absorption of the longitudinal acoustic wave in <110> direction, on the other hand, is governed by its interaction with

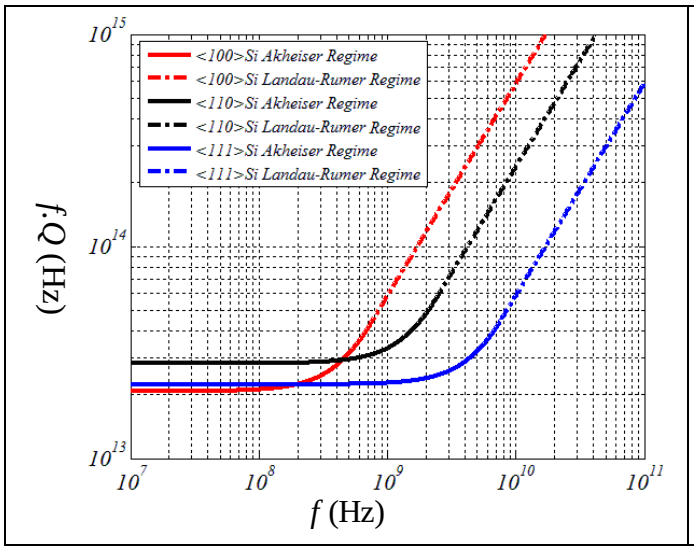

Figure 7. Comparison of fQ_{PhP} for acoustic waves propagating in different crystallographic directions in silicon. The value of $\omega_\tau = 1/\tau$ is extracted from the data for τ presented in [20].

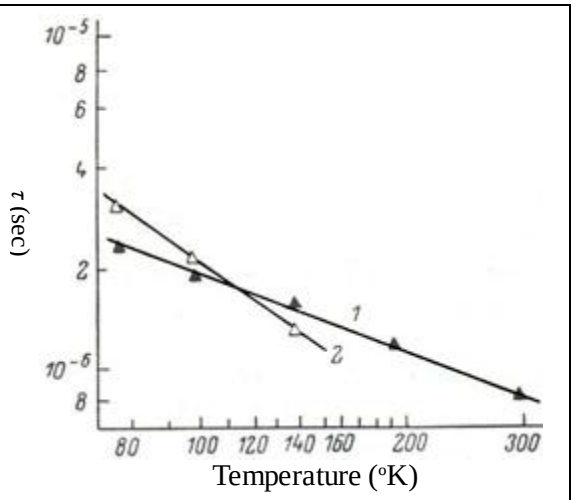

Figure 8. Temperature dependence of the acoustic phonon relaxation time (1) longitudinal in <100> and (2) longitudinal in <110> (figure reproduced from [12])

longitudinal thermal phonons only [17]. Hence, the relaxation time of thermal phonons depends on its interaction with transverse phonons in <100> direction, and with longitudinal phonons in <110> direction. The life time of transverse thermal phonons decreases less rapidly with increasing temperature (Fig. 8). Therefore, at room temperature, τ in <100> direction in silicon remains larger, while in other directions, τ decreases significantly.

To demonstrate the significance of phonon-phonon interactions on limiting the fQ product of a semiconducting or insulating micromechanical resonator, fQ_{PhP} of <100> silicon is compared with that of diamond, AlN, and SiC (shown in Fig. 9). At f > 3 GHz, fQ of <100> Si becomes comparable to that of SiC, which makes the realization of ultra-high-frequency high-Q resonators in silicon possible.

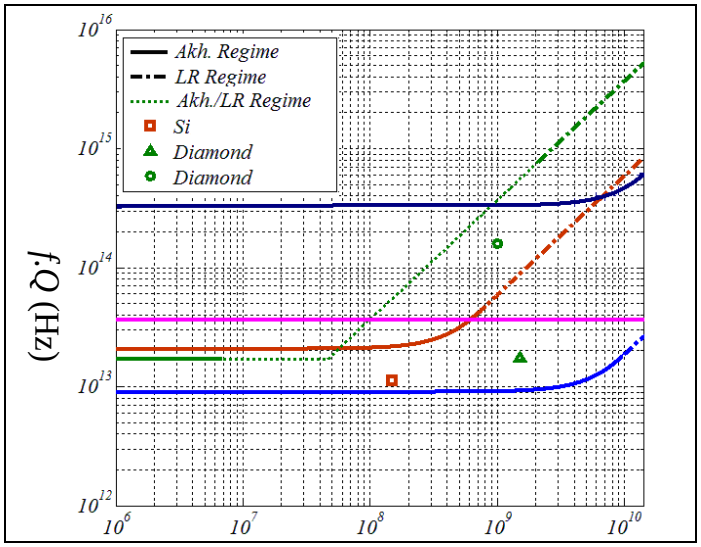

Figure 9. Comparison of $f.Q_{PhP}$ of <100> Si with SiC, AlN, Quartz, and diamond. The highest f.Q product reported for Si and diamond resonators is presented in [18] and [19]. Reference [16] is from measured data for $\alpha(\omega)$ at 1 GHz.

The equation for ω_τ (9) also suggests that high thermal conductivity materials such as diamond experience the Landau-Rumer effect at low frequencies. The measured data for $\alpha(\omega)$ of diamond [21] as well as the analytical calculation of ω_τ presented in [22] support this statement (see Fig. 9).

3. Post-fabrication electrical trimming of silicon bulk acoustic resonators using Joule-heating

Silicon micromechanical resonators have been gaining importance in recent years owing to their small form factor, ease of integration and high *fQ* products. However, the resonance frequency of silicon micromechanical resonators is dependent on the physical dimensions of the resonating structure, which causes it to deviate from its designed target value because of variations in photolithography, etching and film thickness. It can be shown that 2 μm variations in the thickness of an optimized 100 MHz width-extensional-mode SiBAR can cause 0.5% variation in its center frequency [4], while lithographic variations of ±0.1 μm in the width of the resonator can cause additional 0.5% frequency variations.

Electrostatic voltage tuning of high frequency SiBARs is inefficient due to the large stiffness of the device [3] and heat-induced continuous current tuning of the device consumes large power [25]. In addition, these tuning techniques are limited in their tuning range and cannot be used to adjust the resonance frequency in case of large offsets (~1 %), which are quite typical in microfabrication. It is also well known that the frequency of mechanical resonators can be shifted downwards by deposition of a mass loading layer such as a metal on the surface of the resonating structure [26]. However, the thickness of the mass loading layer cannot be accurately controlled, and is subject to the limitations of the metal evaporation systems. Though laser trimming [27] has been shown to shift the resonance frequency of silicon resonators downwards or upwards, the trimming is not precise as it is difficult to control the amount of material deposited or removed by the laser. This calls for an efficient post-fabrication trimming technique which can adjust the resonance frequency precisely to compensate for all possible inaccuracies that stem from the microfabrication processes.

We developed a trimming process whereby a thin-film layer of gold is evaporated and patterned on the surface of a SiBAR during its fabrication. After the resonator is packaged, the SiBAR is heated up by passing a relatively large current through its resonating body during an electrical calibration step, as illustrated in Fig. 10. High current densities due to the small cross-section area of the SiBAR create enough Joule heating to enable the diffusion of gold into the bulk of the silicon resonator. The advantage of gold over other metals is that gold diffuses into silicon at a much lower eutectic temperature of the silicon-gold binary system (360˚C), which is very low compared to the individual melting points of gold (1064˚C) and silicon (1414˚C).

To calculate the temperature of a 100 MHz SiBAR for various durations of Joule heating with a given cross section area (41.5 μm × 20 μm) and resistivity (0.01 Ω-cm), the electro-thermal model based on the conservation of energy was used [28][29]. As discussed later, a silicon beam of such dimensions can be heated to the eutectic temperature in less than five minutes by using currents of 600 mA or more. However, the maximum value of the current in the case of a SiBAR is limited by the small cross-section area of its two narrow supports (illustrated in Figure 10(a)). These supports are designed to be as narrow as possible to reduce acoustic loss and achieve high *Q*, which causes increased current densities at the

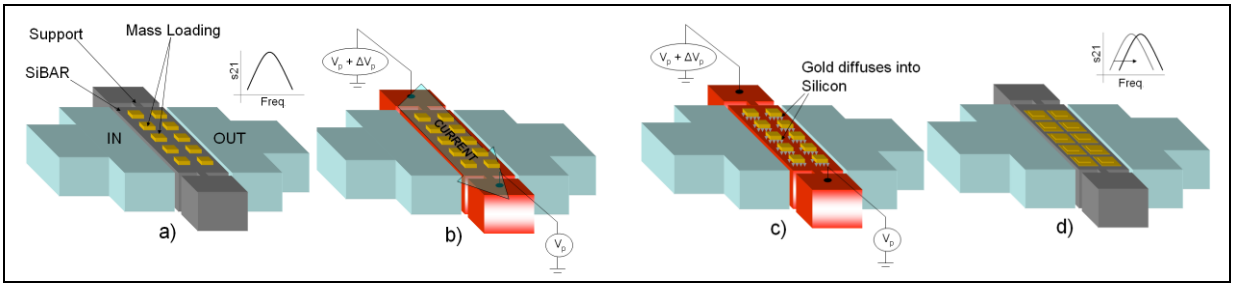

Figure 10: Schematic of electrical trimming of SiBAR using Joule heating; (a) Mass-loaded SiBAR; (b) Joule heating by passing a current through the body of the resonator; (c) Diffusion of gold into silicon; (d) Gold diffused SiBAR at room temperature shows an upward shift in frequency.

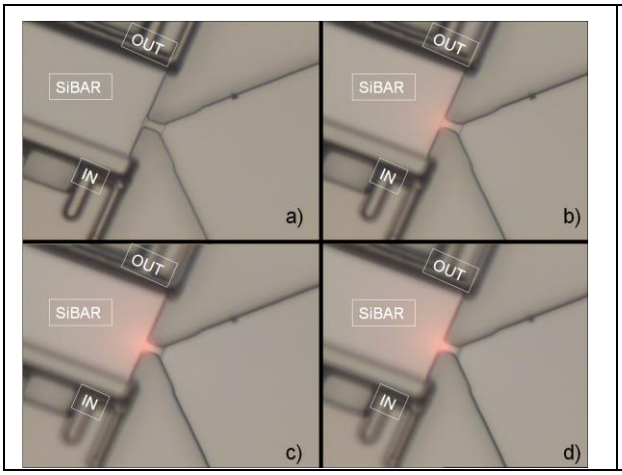

Figure 11: Optical images of Joule heating of the SiBAR at 30 mA after (a) 1 hour (b) 2 hours (c) 3 hours (d) 4 hours.

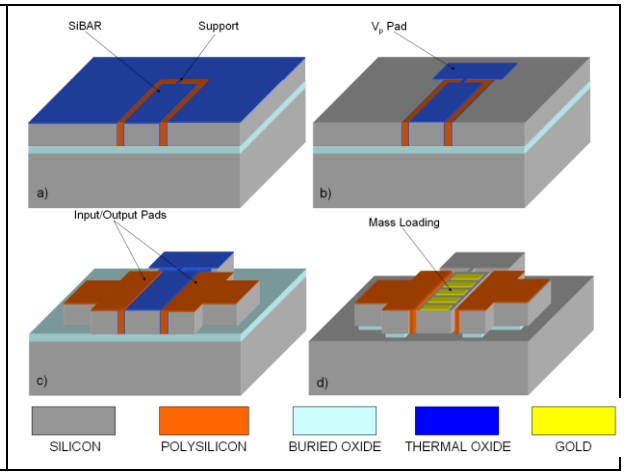

Figure 12: Fabrication process flow of mass-loaded SiBAR.

support regions leading to higher temperatures that can melt the supports. As a proof of concept, an optimum current of 30 mA was found to create the required Joule heating for gold diffusion without affecting the performance of the SiBAR under test and within reasonable lengths of time. The glow color due to Joule heating can be seen by placing the SiBAR under an optical microscope, as shown in Fig. 11. It can be seen that the glow is maximum at the support regions indicating that they heat up the most, as expected. The supports can be made wider to pass higher current to reduce the duration of Joule heating, but at the cost of reducing the *Q* factor.

About one hour of Joule heating heats up the SiBAR to 363˚C, which will favor the formation of the silicon-gold eutectic. The thin mass-loading gold layer will diffuse into the bulk of the silicon at this temperature to form a eutectic alloy which has 19% silicon by atomic weight [30]. As gold atoms diffuse into silicon, they initially form a metastable gold-silicide [31][32], wherein gold gets into the silicon interstitials, breaking Si-Si bonds and creating voids owing to its relatively larger atomic size. Upon further heating, supersaturation occurs followed by decomposition of the gold-silicide to a more stable polysilicon with intermediate voids and Au-Si bonds. The Au-Si bonds are stronger than the Si-Si bonds they replace [33]. As a result, the gold diffusion increases the stiffness (E) of the resonating silicon structure upon cooling. However, the voids introduced in silicon due to gold diffusion reduce its density (ρ). These collectively increase the acoustic velocity of the resonating structure which corresponds to a higher resonance frequency. Thus, the SiBAR can be permanently trimmed to a desired value with mass loading by gold followed by an electrical calibration step. With further Joule heating, the structure stabilizes more until no metastable structure exists.

The fabrication process of the SiBAR is similar to the one reported in [3]. Trenches are etched into the device layer of a 20 µm thick SOI using an oxide mask (Fig. 12(a)). These trenches define the dimensions of the SiBAR and its supports. The 100 MHz SiBARs are 41.5 µm wide and 415 µm long. The supports are 3 µm wide and 6 µm long. The capacitive gap of the SiBAR is defined by the thickness of the grown thermal oxide. In this case, a capacitive gap of 100 nm is obtained.

The trenches are refilled with doped LPCVD polysilicon and are etched back to the surface. The oxide on the surface is patterned (Fig. 12(b)) to define the shape of the polarization voltage (V_p) pads. Input/Output pads are patterned through a second doped LPCVD polysilicon layer (Fig. 12(c)), and the remaining silicon is etched back to the BOX layer of the SOI to isolate input/output and Vp pads. Gold is evaporated and patterned (Fig. 12(d)) on the SiBAR surface using a lift-off process. Gold is deposited on silicon

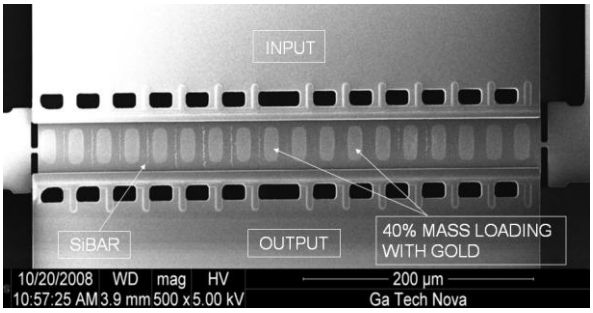

Figure 13: A SEM image of a 40% mass-loaded SiBAR.

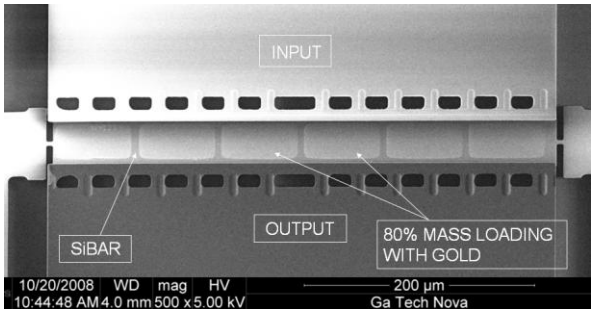

Figure 14: A SEM image of a 80% mass-loaded SiBAR.

without any adhesive layer as that will hinder the gold diffusion into the SiBAR. Finally, the device is released in hydrofluoric acid.

ANSYS predicted a 1 MHz downshift in frequency for a blanket deposition of 150 nm thick gold layer on the entire surface of the SiBAR, referred to in this work as 100% mass loading. Every 10% mass loading results in a 100 kHz downward shift in frequency. The SEM images of the 40% and 80% mass-loaded SiBARs are shown in Figs. 13 and 14. The different pattern densities of gold can be clearly seen.

Figure 15 shows the measured frequencies of various mass-loaded SiBARs before and after trimming via Joule heating. All devices were tested in vacuum and a DC current of 30mA was used for post-fabrication trimming of the resonators.

In Fig. 15, the curve labeled as 'Pre-Joule-Heating' shows the downward shift in frequency due to the mass-loading with various pattern densities of 150 nm thick gold. The 100% mass-loading offers a downward shift of 996.2 kHz in resonance frequency which is in very good agreement with ANSYS simulations. At a polarization voltage of 15 V, the unloaded SiBAR has a Q of 48,000. The mass loading lowers the Q to 23,000 in 40% and to 18,000 in 100% mass-loaded devices.

One hour of Joule heating at 30 mA shifts up the 40% mass loaded SiBAR with smaller islands of gold by 240 kHz and 80% mass loaded SiBAR with larger islands of gold by 17 kHz. This suggests that the localized heating of the SiBAR diffuses smaller islands of gold more readily than larger islands thereby showing larger frequency shifts than the later.

It can also be seen that, for a given mass-loaded SiBAR, the percentage increase in resonance frequency decreases with increasing durations of Joule heating. As explained earlier, the diffusion occurs mainly in the first hour of Joule heating, when the eutectic temperature is reached. Subsequent heating leads to a more stable resonating structure which will correspond to smaller frequency shifts. Hence, four hours of Joule heating shifts up the 40% and 80% mass loaded SiBAR by only 430 kHz and 35 kHz respectively. A shift of 430 kHz over four hours corresponds to a trimming rate of approximately 2 kHz per minute, which makes very precise and controlled electrical trimming possible.

The 40% mass loaded SiBAR is designed to give a resonance frequency of 99.6 MHz (i.e., a downshift of 400 kHz from 100 MHz). But it can be seen that variations in the SiBAR fabrication and also in the thickness of the deposited gold offsets the resonance frequency to 99.46 MHz. The electrical trimming time needed to shift up this frequency to the designed 99.6 MHz can be calculated to be 35 minutes from Fig. 15. Thus, all variations of the SiBAR fabrication can be compensated successfully. From Fig. 15 it can also be seen that the 40% mass loaded SiBAR exceeds the resonance frequency of unloaded SiBAR with longer hours of Joule heating. This suggests the formation of a structure with stronger Au-Si bonds and less dense packing with voids, to provide a higher acoustic velocity than crystalline silicon.

After electrical trimming, these devices were taken through temperature cycling by heating them in an oven to 85˚C for 6 hours and back to room temperature. No frequency hysteresis was observed,

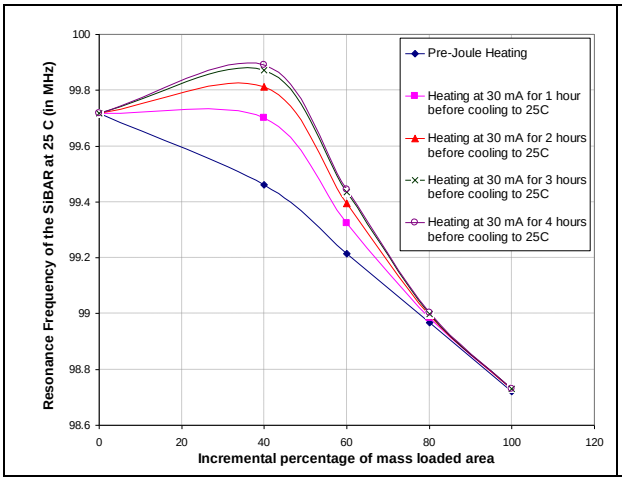

Figure 15: Measured post-fabrication electrical trimming of the SiBAR using Joule heating.

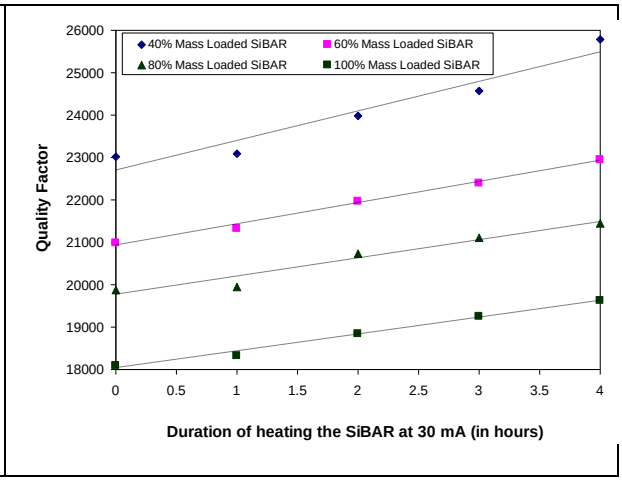

Figure 16: Measured increase in the Q of the mass loaded SiBAR versus duration of Joule heating.

confirming the temperature stability of the trimmed resonator. Although mass loading reduces the *Q* of a SiBAR from its unloaded pure-silicon value, Fig. 16 shows that the *Q* increases slightly with longer hours of Joule heating.

4. Temperature compensation via degenerate doping and electromigration

Silicon micromechanical resonators rely on the propagation of longitudinal or shear elastic waves through the resonating silicon bulk. Such an acoustic wave propagating through the silicon bulk acoustic resonator distorts the energy valleys in *k*-space in the conduction band of silicon [34] creating an electron flow from higher to lower energy valleys (the same principle applies to holes), thereby varying the total electronic energy of the system. This variation is a function of temperature and manifests itself as a corresponding change in the total elastic energy of the system which gives rise to a TCF in silicon resonators. At degenerate levels of doping, the dopant energy levels could potentially be filled with free carriers, which shield the acoustic wafer from *k*-space contours of the conduction bands [35] thereby providing TCF compensation. We have demonstrated TCF compensation in p-type silicon resonators using degenerate boron doping and boron-assisted aluminum doping.

Silicon bulk acoustic resonators (SiBAR) were fabricated using the HARPSS process [3] on a 10 µm thick boron-doped silicon wafer as purchased from the vendor, with a starting resistivity of ~10^{-2} Ω-cm and a TCF of –29 ppm/˚C. The resistivity of silicon was measured using *Signatone Four Point probe station*. The resistivity of silicon was reduced down to ~10^{-3} Ω-cm by repeated doping using solid boron sources. For further reduction in resistivity to obtain degenerate doping levels, repeated doping using liquid spin-on boron dopant sources were needed.

Table III: Comparison of Boron doping recipe using solid and liquid boron sources

Boron Dopant Type	Dope Recipe	Anneal Recipe	HF dip
Solid Boron Disks	3 hours in furnace at 1050 ˚C	5 hours at 1100 ˚C in N_2	-Yes-
Liquid Boron Spin-on-Dopants	Spin dopant at 800 rpm for 40s / Bake at 200 ˚C for 3 min.	8 hours at 1100 ˚C in N_2	-Yes-

Table III illustrates the boron doping recipes using solid and liquid boron sources. The silicon wafer with the starting resistivity of ~10^{-2} Ω-cm was first doped using solid boron disks as the diffusion source in a Tystar furnace. Every cycle of doping involved 3 hours of doping at 1050 ˚C followed by 5 hours of annealing at 1100 ˚C in nitrogen ambient and HF dip to remove the borosilicate glass (BSG). After five such

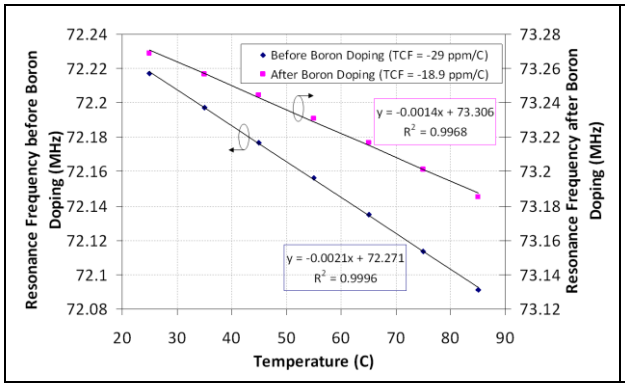

Figure 17: TCF measurements before (10^{-2} Ω-cm) and after (10^{-3} Ω-cm) boron doping (using solid boron sources) on a 10 µm thick SiBAR.

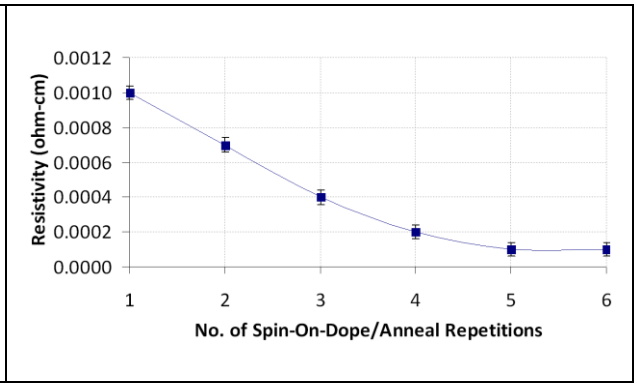

Figure 18: Four-point probe measurement of reduction in resistivity from 10^{-3} Ω-cm to 10^{-4} Ω-cm for every repetition of Spin-On-Dope/Anneal processes

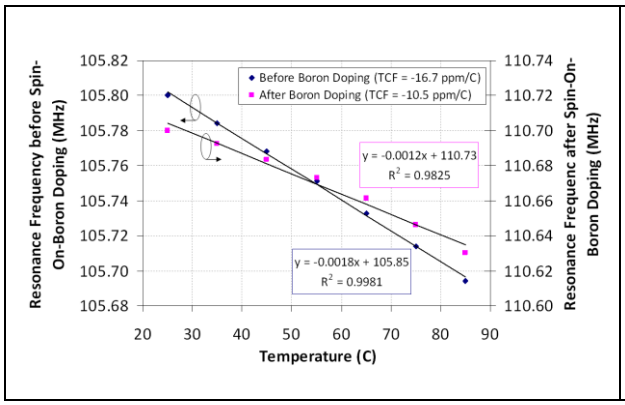

Figure 19: TCF Measurements before (10^{-3} Ω-cm) and after (10^{-4} Ω-cm) boron doping (using liquid boron sources) on a 10 µm thick SiBAR

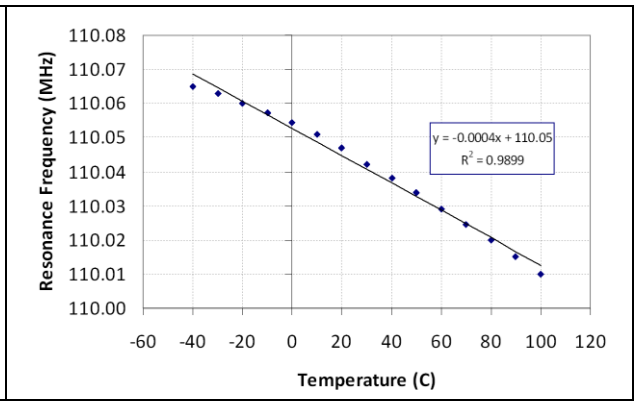

Figure 20: TCF measurements of a 5 µm thick SiBAR after doping with liquid boron sources (10^{-4} Ω-cm), showing a TCF of -3.56 ppm/°C

cycles, the silicon resistivity was reduced to ~10^{-3} Ω-cm and a corresponding TCF of –18.9 ppm/˚C was measured (Fig. 17).

As seen from the square of the correlation co-efficient of linearity (R^2) reported in Fig. 17, the linearity of the TCF curve is compromised due to the boron doping. For further reduction of silicon resistivity, Spin-on-Dopant (SOD) boron sources [*Futurrex Inc.*, *BDC1-2000*] were used. Every cycle of doping involved spinning of liquid boron dopants at 800 rpm for 40 seconds and baking at 200 ˚C to evaporate solvents followed by 8 hours of annealing at 1100 ˚C in nitrogen ambient and HF dip to remove the borosilicate glass (BSG). After six such cycles, the silicon resistivity was further reduced to 10^{-4} Ω-cm (Fig. 18). A reduction in TCF from –16.7 ppm/˚C at 10^{-3} Ω-cm to –10.5 ppm/˚C at 10^{-4} Ω-cm was measured (Fig. 19). The increase in resonance frequency after doping is due to the increase in Young's modulus of silicon and is indicative of degenerative doping [37]. The maximum thickness of the heavily boron doped layer that can be achieved using SOD is limited to 7~8 µm [36] which leads to a non-uniform doping profile in SiBARs thicker than 8 µm. However, a 5 µm thick SiBAR with a resistivity of ~10^{-4} Ω-cm measured a much lower TCF of 3.56 ppm/˚C (Fig. 20) indicating a uniform doping profile along its thickness. Further repetition of the Spin-on-Dope/Anneal cycles reduces the TCF to –1.5 ppm/˚C and not any lower (Fig. 21).

It is known [38] that the frequency variation with temperature in silicon micromechanical resonators is due both to the temperature coefficient of Young's modulus and to the linear thermal expansion coefficient of the resonator material. The first effect is dominant, while the second contributes only ~1.5

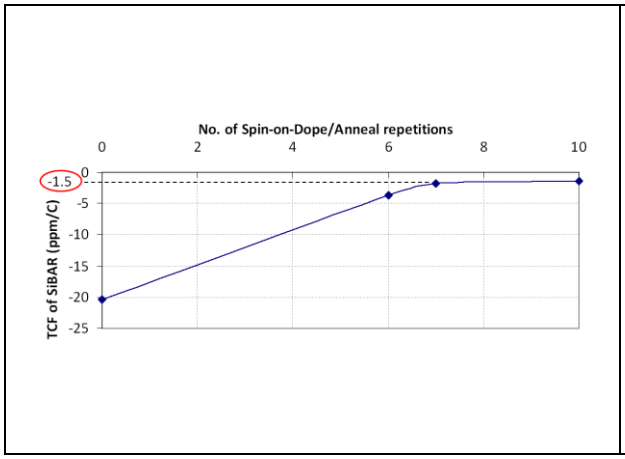

Figure 21: Saturation of TCF at ~-1.5 ppm/˚C of the 5 µm thick SiBAR after 7 repetitions of Spin-on-Dope/Anneal processes.

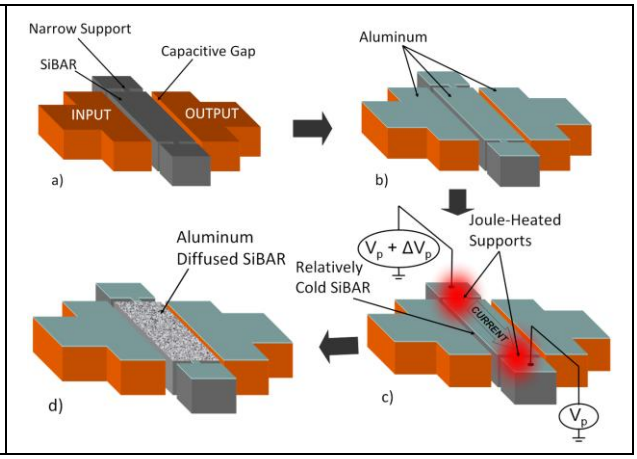

Figure 22: Schematic of aluminum thermomigration into SiBAR for TCF reduction.

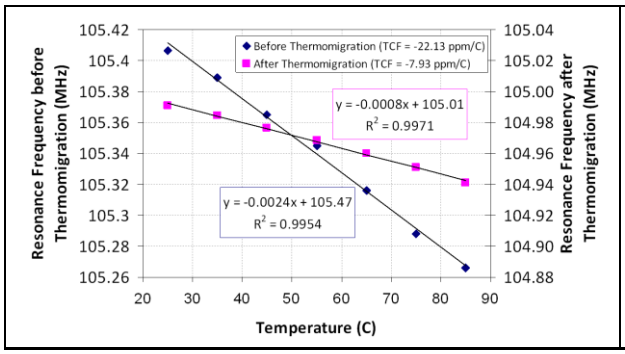

Figure 23: TCF Measurements of a 20 µm thick [10^{-3} Ω-cm boron-doped] SiBAR before and after thermo-migration with 500 Å of aluminum @ 120 mA for 10 minutes

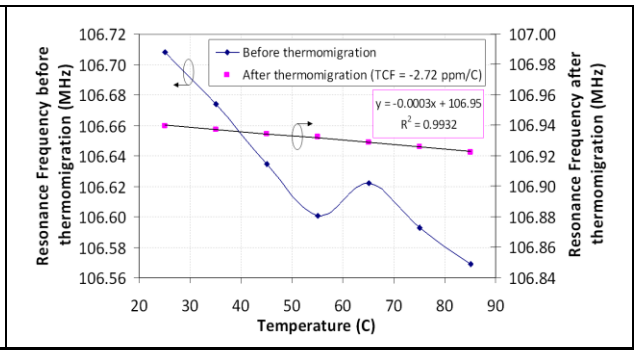

Figure 24: TCF Measurements of a 20 µm thick [10^{-4} Ω-cm boron-doped] SiBAR before and after thermo-migration with 500 Å of aluminum at 120 mA for 10 minutes

ppm/˚C to the total TCF value. This is also verified by setting the thermal coefficient of expansion (TCE) value of the orthotropic silicon model in ANSYS to 0 while simulating the TCF of the SiBAR. Such an ANSYS simulation predicts a TCF value of –1.2 ppm/˚C which is in very close agreement with the lowest measured TCF values via degenerate boron doping. Hence, it is inferred that degenerate boron doping compensates for all of the frequency variation contributed by the temperature coefficient of Young's modulus and the measured residual TCF of –1.5 ppm/˚C stems from the linear thermal expansion coefficient of the resonating doped-silicon material. Thus, an overall reduction in TCF from –29 ppm/˚C to –1.5 ppm/˚C can be achieved in silicon micromechanical resonators using degenerate boron doping. However, the long hours of annealing required for achieving degenerate boron doping and the limited thickness of such achievable heavily doped boron layers are some of the drawbacks of this technique.

Boron diffuses as an interstitial dopant [39], which demands for longer hours of annealing to become electrically active. On the other hand, aluminum (a p-type dopant) becomes readily electrically active by diffusion via self-interstitial mechanism [40]. Aluminum can be thermomigrated against a temperature gradient into hundreds of microns thick silicon within few tens of minutes [41].

Additionally, the uniformity and speed of aluminum thermomigration is enhanced by the presence of boron atoms in silicon [40]. Thus, *boron-assisted aluminum thermomigration* is a faster alternative to degenerate boron doping for TCF reduction. This was investigated by evaporating a thin layer of

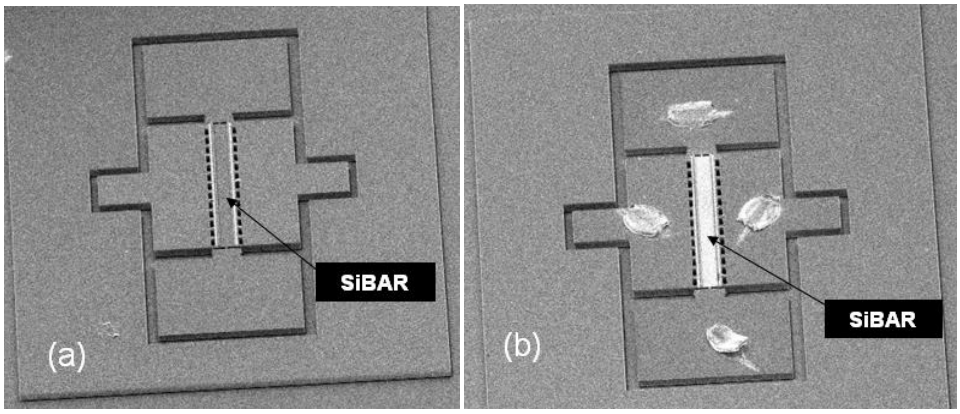

Figure 25: SEM images of the SiBAR reported in Fig. 24 (a) before and (b) after thermomigration with 500 Å thick aluminum at 120 mA for 10 minutes. The charging up of the SiBAR under the SEM after aluminum thermomigration indicates that the aluminum has diffused completely from the surface of the SiBAR into the bulk. Wirebond traces are visible in (b) since the same device was used for SEM images.

aluminum onto the SiBAR and the narrow support elements are Joule-heated [42] by passing a current through the SiBAR resonator element (Fig. 22). Aluminum on top of the relatively cold SiBAR diffuses through the silicon towards the hot support elements thereby doping it. 500 Å of aluminum was evaporated onto a boron-doped 20 µm thick SiBAR with a starting resistivity of ~10^{-3} Ω-cm. Thermomigration was performed by passing a current of 120 mA through the SiBAR for 10 minutes after which the TCF reduces from –22.13 ppm/˚C to -7.93 ppm/˚C (Fig. 23). A similar thermomigration performed on the degenerate boron-doped (~ 10^{-4} Ω-cm) 20 µm thick SiBAR yields a TCF as low as –2.72 ppm/˚C ('After' curve in Fig. 24). The 'Before' curve in Fig. 24 shows an anomalous behavior due to the non-uniform boron doping profile along the 20 µm thickness of the SiBAR.

Such low-TCF is obtained via boron-assisted aluminum thermomigration without compromising on the quality factor (*Q*) of the resonator which is measured to be 28000 in vacuum [43]. The SEM images of this SiBAR before and after thermomigration are shown in Fig. 25.

5. Temperature compensation via resonator geometry engineering

The momentary strain produced by the propagation of an acoustic wave through silicon distorts and splits the equivalent energy surfaces of the electronic band structure [34]. As a consequence, free charge carriers flow towards more energetically favorable energy levels thereby shifting the Fermi level of the semiconductor. The amount of free charge carrier flow and the resulting shift in Fermi level (and thereby the total electronic energy) increases with temperature. The principle of conservation of energy requires that such a temperature dependant change in the electronic energy of the system manifest itself as a corresponding temperature dependant change in the elastic energy of the system, which causes a negative TCE in silicon. However, by creating a relatively larger strain in the resonating microstructure, the effect of strain from the acoustic waves can be made minimal in comparison thereby achieving temperature compensation. The introduction of a dopant like boron or aluminum which has an atomic radius smaller than silicon, a large shearing strain can be created in the silicon atomic lattice. We have shown that such a large stain was sufficient to reduce the TCF to as low as ~–1.5 ppm/˚C at a degenerate boron-doped silicon resistivity of ~10^{-4} Ω-cm [43].

A similar large strain can also be created by introducing shear acoustic waves in the resonator along with the longitudinal waves already existing in the width-extensional mode of the SiBAR. By engineering the resonator geometry and placement of electrodes, a mixture of both longitudinal and shear waves can be actuated wherein the later could be utilized for TCF reduction. Figure 26(a) introduces the Concave Silicon Bulk Acoustic Resonator (CBAR) which is realized by curving the long edges of the conventional

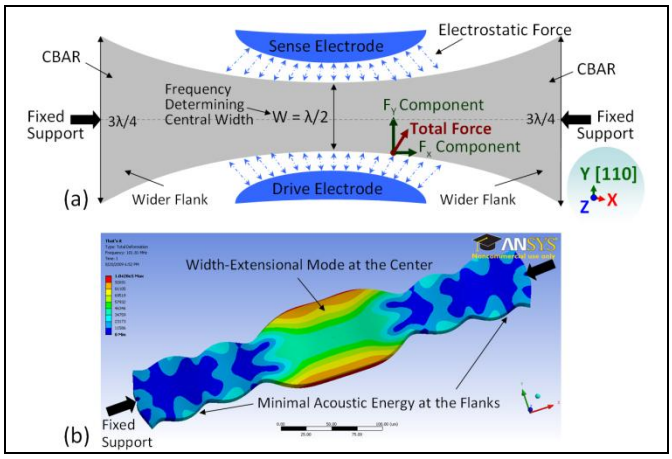

Figure 26: (a) Schematic and (b) simulated width-extensional mode of a Concave Silicon Bulk Acoustic Resonator (CBAR)

rectangular Silicon Bulk Acoustic Resonator (SiBAR) such that the central width remains λ/2 but has wider flanks on either side. The electrodes are designed with the same curvature as that of the CBAR The electrostatic force applied normal to the curved CBAR surface by the electrodes can be resolved into its corresponding tensile (F_Y) and shear force (F_X) components as illustrated in Fig. 26(a). The ensemble of the tensile forces actuates the WEM of the CBAR (Fig. 26(b)) whereas the shear force elements actuate shear waves that contribute to the additional shearing strain in the microresonator. Additionally, the flank width, when made exactly equal to 3λ/4, acts as a sink for the acoustic energy at the resonance frequency determined by the central width of λ/2. Such a resonator design concentrates the acoustic energy near the central region (Fig. 26(b)) thereby minimizing the acoustic loss at the narrow support elements and hence enhancing the *Q* of the resonator.

Figure 27 compares the longitudinal and shear strain in a SiBAR and CBAR. Figure 27(a) shows an increased longitudinal strain along *Y* direction in the width-extensional mode of the CBAR compared to that of the SiBAR due to the concentration of acoustic energy near the center in a CBAR. However, the longitudinal strain along X axis and the shear strain along the XY plane, which are insignificant in the

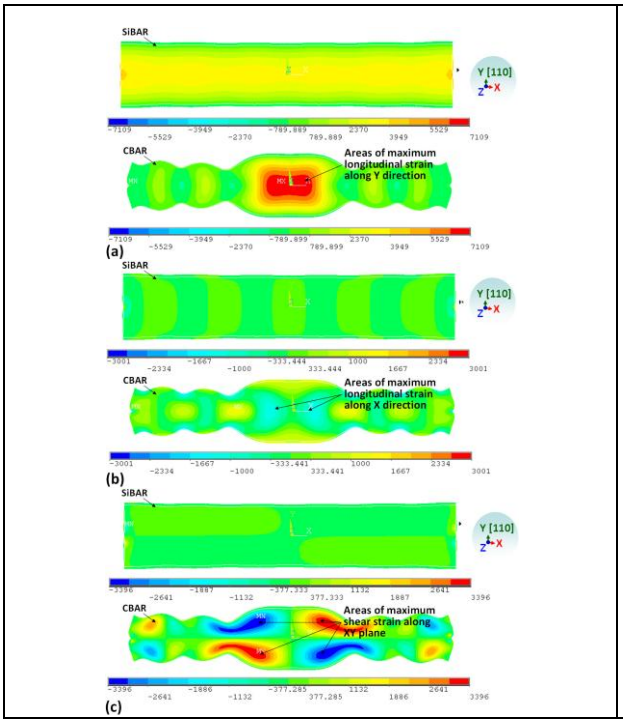

Figure 27: Simulated longitudinal strain along (a) Y and (b) X axes and shear strain along the (c) XY plane of a SiBAR vs CBAR.

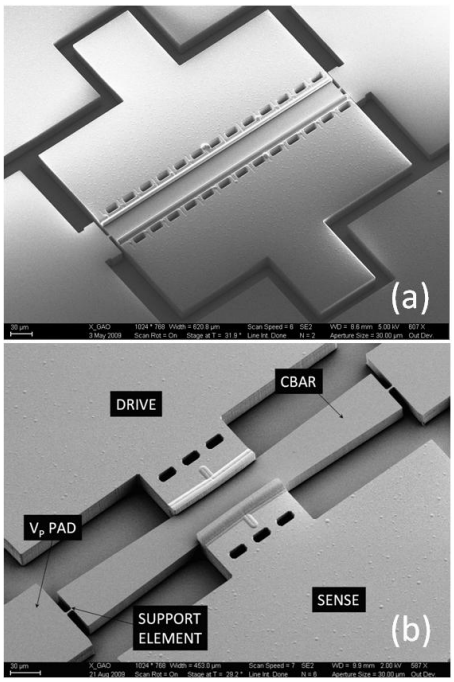

Figure 28: SEM image of (a) a Conventional SiBAR and (b) a Concave SiBAR (CBAR) with central width 40 μm (λ/2); flank width = 60 μm (3λ/4);; thickness = 20 μm and length = 400 μm, fabricated on a ~10^{-3} Ω-cm silicon wafer

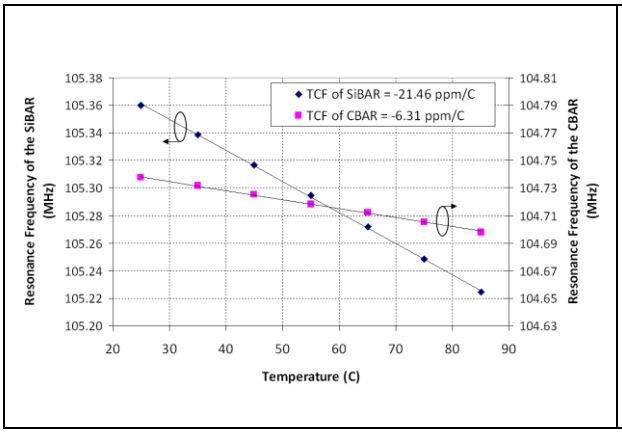

Figure 29: Measured TCF of SiBAR & CBAR fabricated on a ~10^{-3} Ω-cm wafer .

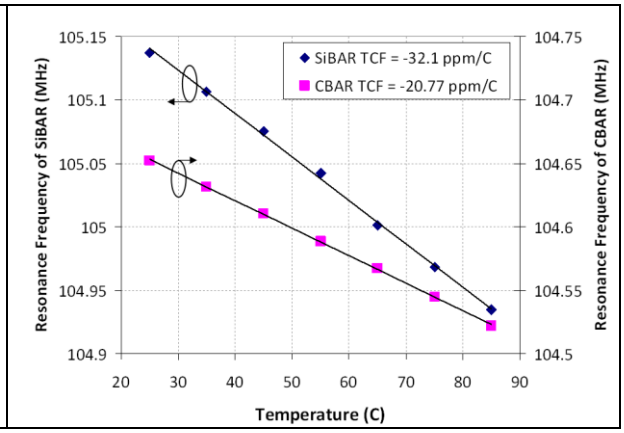

Figure 30: Measured TCF of SiBAR & CBAR fabricated on a >1000 Ω-cm wafer

SiBAR, are very strongly pronounced in the CBAR structure (Figs. 27(b) and 27(c)). These strain components create a larger strain in the actively transduced central region of the CBAR compared to the longitudinal strain along the Y axis. The former are responsible for the reduction in TCF of the CBAR whereas the later transduces as the output at the electrodes. ANSYS predicts that such a CBAR structure offers a reduction in TCF by 13 ppm/°C compared to that of the SiBAR.

To demonstrate TCF reduction and *Q* enhancement, 100 MHz SiBAR and CBAR were fabricated on the same boron-doped silicon with a resistivity of ~10^{-3} Ω-cm using the HARPSS process [3] with a capacitive gap of 100 nm. Unlike a SiBAR, the drive/sense electrodes are positioned only around the actively transduced central region of the CBAR as shown in Fig. 28. As shown in Fig. 29, the TCF of the CBAR is measured to be –6.31 ppm/°C, which is 15 ppm/°C smaller than a SiBAR fabricated on the same wafer.

Further, the measured response of the CBAR in vacuum shows a *Q* of 101,000 at 104.92 MHz, which makes it the first silicon micromechanical resonator reported with a TCF as low as –6.31 ppm/°C while maintaining an *fQ* product of over 1.06×10^{13} [44].

To assess the influence of the ultra-low resistivity substrate on the achieved TCF values, the SiBAR and CBAR were also fabricated on a boron-doped wafer with ultra-high resistivity of >1000 Ω-cm. Such a CBAR measured a TCF of –20.77 ppm/°C which was still 12 ppm/°C lower than the TCF of a SiBAR from the same wafer (Fig. 30). This confirms the engineering of the resonator geometry and electrode placement as a viable passive technique for achieving TCF compensation in silicon micromechanical resonators with a potential for simultaneous *Q* enhancement.

As explained in Section 4, aluminum thermomigration provides a faster, more convenient alternative to degenerative doping for the purpose of temperature compensation. Aluminum, like boron, is a p-type dopant that has a smaller radius than silicon. Therefore, the resulting shearing strain due to aluminum thermomigration provides temperature compensation. However, aluminum can be thermomigrated against a temperature gradient into hundreds of microns thick silicon within few tens of minutes [41].

This was investigated by evaporating 200 Å of aluminum onto the SiBARs fabricated on ~ 10^{-2} Ω-cm silicon. The required temperature gradient is created in a furnace by turning off one of the many coil heaters. The wafer is positioned in the furnace at the boundary of the hot and cold regions, with the aluminum deposited side facing away from the heat. The temperature gradient across the thickness of the wafer drives the aluminum to thermomigrate into the resonating silicon bulk. After one hour of thermomigration in nitrogen ambient, the residual aluminum on the surface of the resonators was

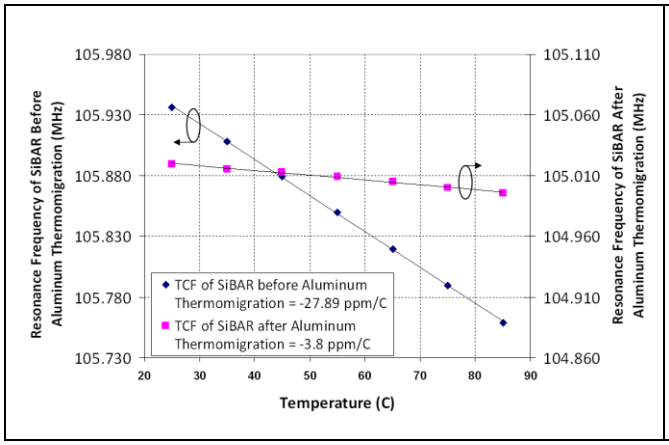

Figure 31: Wafer-level TCF reduction in ~10^{-2} Ω-cm SiBAR after one hour of aluminum thermomigration

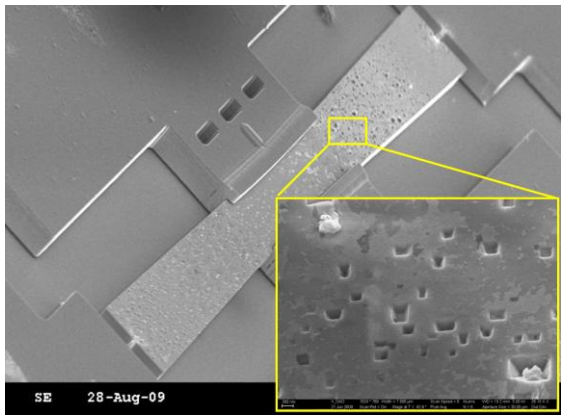

Figure 32: Induced stress and lattice damage in a CBAR after 30 minutes of aluminum thermo-migration.

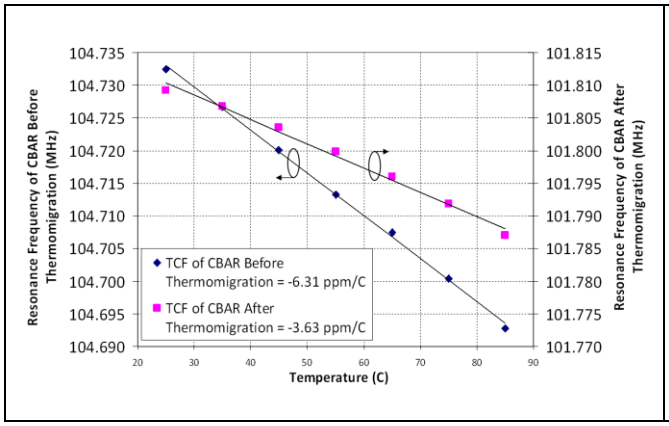

Figure 33: Wafer-level TCF reduction in ~10^{-3} Ω-cm CBAR after 30 minutes of aluminum thermomigration

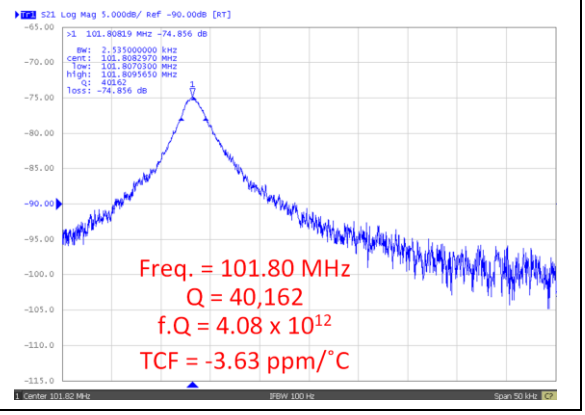

Figure 34: Measured frequency response in vacuum of a ~10^{-3} Ω-cm CBAR after 30 minutes of aluminum thermomigration

removed using hydrofluoric acid. The TCF of the SiBAR reduced from –27.8 ppm/°C to –3.8 ppm/°C (Fig. 31).

The rapid thermomigration process and the large temperature gradient across the thickness of the devices were found to induce stress and lattice damage to the resonating structure. As a result, the *Q* of the SiBAR reduces by an order of magnitude to ~10,000 in vacuum at 100 MHz. However, the inherent high *Q* of the CBARs withstands the lattice damage better than the SiBARs. Thermomigration was performed on the CBARs of Fig. 29 with a starting resistivity of ~10^{-2} Ω-cm. The resulting lattice damage is illustrated in Fig. 32. Upon thermomigration for 30 minutes, the TCF of the CBAR further reduces from –6.31 ppm/°C to –3.63 ppm/°C (Fig. 33) with a *Q* of 40,000 in vacuum which has an *fQ* of 4 x 10^{12} (Fig. 34).

REFERENCES

[1] J. Wang, Z. Ren and C. T.-C. Nguyen, "Self-aligned 1.14 GHz vibrating radial-mode disk resonators," in *Proc. TRANSDUCERS 2003*, vol. 2, pp. 947–950.

[2] S. Pourkamali, G.K. Ho and F. Ayazi, "Vertical capacitive SiBARs," in *Proc. MEMS 2005*, pp. 211–214.

[3] S. Pourkamali, G. K. Ho and F. Ayazi, "Low-impedance VHF and UHF capacitive silicon bulk acoustic wave resonators – Parts I and II," *IEEE Trans. Electron Devices*, vol. 54, no. 8, pp. 2017–2030, Aug. 2007.

[4] G. Casinovi, X. Gao and F. Ayazi, "Analytical modeling and numerical simulation of capacitive silicon bulk acoustic resonators," in *Proc. MEMS 2009*, pp. 935–938.

[5] G. K. Ho, "*Design and Characterization of Silicon Micromechanical Resonators*," Ph. D. Thesis, Georgia Institute of Technology, 2008.

[6] S. A. Chandorkar, et al., "Limits of quality factor in bulk-mode micromechanical resonators," *Proc. IEEE MEMS*, Tucson, AZ, Jan. 2008, pp. 74-77.

[7] V. B. Braginsky, et al., *Systems with Small Dissipation*, The University of Chicago Press, 1985.

[8] Z. Hao, A. Erbil, and F. Ayazi, "An Analytical Model for Support Loss in Micromachined Beam Resonators with In-plane Flexural Vibrations," *Sensors and Actuators A*, vol. 109, Dec. 2003, pp. 156-164.

[9] L. D. Landau and E. M. Lifshitz, *Theory of Elasticity*, Linarce House, Oxford, 3rd ed., 1986.

[10] A. Akheiser, *J . Phys. USSR*, pp. 1277, 1939.

[11] T. O. Woodruff and H. Ehrenreich, "Absorption of sound in insulators," *Phys. Rev.*, pp. 1553-1559, Sep. 1961.

[12] L. Landau and G. Rumer, *Phys. Z. Sowjetunion* 11, 18, 1937.

[13] Y. Shapira, B. Fisher, B. Pratt, and A. Many, "Measurements of acoustoelectric gain and lattice attenuation in n-GaAs," *J. Phys. C: Solid State Phys.* vol. 5, pp. 3477-3490, 1972.

[14] C. Zener, *Elasticity and Anelasticity of Metals*, The University of Chicago Press, Chicago, Illinois, 1948.

[15] J. F. Rosenbaun, *Bulk acoustic wave theory and devices*, Artec House, Boston-London, 1988.

[16] Yu. A. Logachev and Fiz. Tverd. Tela, *Sov. Phys. Solid State*, vol. 16, pp. 2008, 1975.

[17] Y. V. Ilisavskii and V. M. Sternin, *Sov. Phys. Solid State*, vol. 27, pp. 236-239, February 1985.

[18] J. Hasson and A. Many, "Observation of Akhiezer and Landau-Rumer regions in the frequency dependence of shear-wave lattice attenuation in CdS," *Phys. Review Letters*, v. 35, pp. 792-795, Sept. 1975.

[19] B. C. Daly, K. Kang, D. G. Cahill, "Attenuation of picosecond ultrasonic pulses in a thin silicon wafer," *1st Int. Symposium on Laser Ultrasonics: Science, Technology and Applications*, July 2008, Montreal, Canada.

[20] S. D. Lambade, G. G. Sahasrabudhe, and S. Rajagopalan, "Temperature dependence of acoustic attenuation in silicon," *Physical Review B, Vol. 51, no. 22*, pp. 861-866, 1995.

[21] I. S. Didenko, F. S. Hickernell, and N. F. Naumenko, "The experimental and theoretical characterization of the SAW propagation properties for zinc oxide films on silicon carbide," *IEEE Trans. on Ultrasonics, Ferroelectrics, and Frequency Control*, vol. 47, pp. 179-187, Jan. 2000.

[22] I. G. Kuleyev, I. I. Kuleyev, A. P. Tankeyev, and I. Yu. Arapova, "Landau-Rumer relaxation mechanism of the thermal and high-frequency phonons in cubic crystals," *phys. stat. sol. (c) 1*, no. 11, pp. 2963-2966, 2004.

[23] J. Wang, J. E. Butler, T. Feygelsonand, and C. T.-C. Nguyen, "1.51-GHz nanocrystalline diamond micromechanical disk resonator with material-mismatched isolating support," in *Proc. IEEE Int. Conf. MEMS*, 2004, pp. 731-734.

[24] H. M. Lavasani, A. K. Samarao, G. Casinovi, and F. Ayazi, "A 145MHz low phase-noise capacitive silicon micromechanical oscillator," *Proc. IEEE IEDM*, San Francisco, CA, Dec. 2008.

[25] K. Sundaresan, G. K. Ho, S. Pourkamali and F. Ayazi, "Electronically Temperature Compensated Silicon Bulk Acoustic Resonator Reference Oscillators", *J. Solid State Circuits*, pp. 1425-1434, 2007.

[26] C. G. Courcimault and M. G. Allen, **"**High-Q Mechanical Tuning of MEMS Resonators using a Metal Deposition - Annealing technique", *Transducers 2005*, pp. 875-878.

[27] W- T. Hsu, A. R. Brown, "Frequency Trimming of MEMS Resonator Oscillators", *IEEE Intl. Freq. Control Sym. 2007*, pp 1088-1091.

[28] L. Lin, "Selective encapsulations of MEMS: Micro channels, needles, resonators, and electromechanical filters", Ph.D. dissertation, Dept. Mech. Eng., Univ. California at Berkeley, Berkeley, CA, 1993.

[29] Y. T. Cheng, L. Lin and K. Najafi, "Localized Silicon Fusion and Eutectic Bonding for MEMS Fabrication and Packaging", *J. Microelectromech. Syst.*, vol. 9, pp. 3-8, 2000.

[30] H. Okamoto and T. B. Massalski: *Binary Phase Diagrams* (1986), p. 312.

[31] B. Bokhonov and M. Korchagin, "In Situ Investigation of Stage of the Formation of Eutectic Alloys in Si-Au and Si-Al Systems", *J. Alloys and Compounds*, vol. 312, pp. 238-250, 2000.

[32] S. Takeda, H. Fujii, Y. Kawakita, S. Tahara, S. Nakashima, S. Kohara and M. Itou, "Structure of eutectic alloys of Au with Si and Ge", *J. Alloys and Compounds*, vol. 452, pp. 149-153, 2008.

[33] L. Lin, Y. T. Cheng and K. Najafi, "Formation of Silicon-Gold Eutectic Bond Using Localized Heating Method", *Japanese J. Applied Physics*, vol. 37, pp. 1412-1414, 1998.

[34] P. Csavinszky et al, "Effect of Doping on Elastic Constants of Silicon," *Physical Review Letters*, vol. 132, no. 6, pp 2434-2440, Dec. 1963.

[35] P. Csavinszky et al, "Effect of holes on the elastic constant C' of degenerate p-type Si," *Journal of Applied Physics*, vol.36, no.12, pp 3723-3727, Dec. 1965.

[36] C. Iliescu, et al, "Analysis of highly doping with boron from spin-on diffusing source," *Surface & Coatings Technology*, vol. 198, no. 1-3, pp 309-313, Aug. 2005.

[37] Naoki Ono et al, "Measurement of Young's modulus of silicon single crystal at high temperature and its dependency on boron concentration using flexural vibration method," *Japanese Journal of Applied Physics*, vol. 39, pp 368-371, Feb. 2000.

[38] Z. Hao, S. Pourkamali, and F. Ayazi, "VHF Single Crystal Silicon Elliptic Bulk-Mode Capacitive Disk Resonators; Part I: Design and Modeling," *IEEE Journal of Microelectromechanical Systems*, vol. 13, no. 6, pp. 1043-1053, Dec.2004.

[39] B. Sadigh, et al, "Mechanism of boron diffusion in silicon: an ab initio and kinetic Monte Carlo study," *Physical Review Letters*, vol. 83, no. 21, pp 4341-4344, Nov. 1999.

[40] O. Krause, et al, "Determination of aluminum diffusion parameters in silicon," *Journal of Applied Physics*, vol. 91, no. 9, pp 5645-5649, May 2002.

[41] C. C. Chung and M. G. Allen, "Thermomigration-based junction isolation of bulk silicon MEMS devices," *Journal of Microelectromechanical Systems*, vol. 15, no. 5, pp 1131-1138, Oct. 2006.

[42] A. K. Samarao and F. Ayazi, "Post-fabrication electrical trimming of silicon bulk acoustic resonators using joule heating," *Proc. IEEE MEMS*, pp 892-895, Jan 2009.

[43] A. K. Samarao and F. Ayazi, "Temperature compensation of silicon micromechanical resonators via degenerate doping," *Proc. IEDM*, pp 1-4, Dec. 2009.

[44] A. K. Samarao, G. Casinovi and F. Ayazi, "Passive TCF compensation in high-*Q* silicon micromechanical resonators," *Proc. IEEE MEMS*, pp 116-119, Jan 2010.